Laminar natural convection in a square cavity with 3D random roughness elements considering the compressibility of the fluid

Ren, Boqi

Li, Chung-Gang

Tsubokura, Makoto

(Citation)
International Journal of Heat and Mass Transfer,173:121248

(Issue Date)
2021-07

(Resource Type)
journal article

(Version)
Accepted Manuscript

Laminar natural convection in a square cavity with 3D random roughness elements considering the compressibility of the fluid

Boqi Ren[a], Chung-Gang Li[a,b], Makoto Tsubokura[a,b]

[a]Graduate School of System Informatics, Kobe University,

1-1 Rokkodai, Nada-ku, Kobe, Hyogo 657 8501, Japan

E-mail: bochiren1992@stu.kobe-u.ac.jp

[b]Complex Phenomena Unified Simulation Research Team, RIKEN,

Advanced Institute for Computational Science,

7-1-26 Minatojima-minami-machi, Chuo-ku, Kobe, Hyogo 650-0047, Japan

E-mail: cgli@aquamarine.kobe-u.ac.jp; tsubo@tiger.kobe-u.ac.jp

Correspondence to: Chung-Gang Li

Computational Fluid Dynamics Laboratory

Department of Computational Science

Graduate School of System Informatics

Kobe University, 1-1 Rokkodai, Nada-ku,

Kobe 657-8501, Japan

E-mail: cgli@aquamarine.kobe-u.ac.jp

+81-78-803-6680

Laminar natural convection in a square cavity with 3D random roughness elements considering the compressibility of the fluid

Abstract

Natural convection in a three-dimensional square cavity with random artificial roughness on both vertical walls is studied numerically for a Rayleigh number of 10^6. Based on consideration of realistic conditions, the roughness is generated using a given power spectrum density, and a compressible solver with preconditioning that uses a dual time-stepping method is established to handle the low velocity of the natural convection flow. The compressible solver demonstrates satisfactory accuracy in terms of the average Nusselt number when compared with incompressible benchmark solutions. However, the results for the local Nusselt number from the compressible and incompressible solvers differ. As the temperature difference between the two vertical sidewalls increases, the maximum value of the local Nusselt number increases, but in the downstream region, the local Nusselt number actually decreases. The cavity with rough sidewalls has a similar Nusselt number to the average Nusselt number of a hot sidewall in the case of a smooth cavity. Because of the effects of the roughness on the thermal and velocity boundary layers, the rough cavity case shows a better heat transfer performance than the smooth cavity case in the upstream region, but in the downstream region, the heat transfer in the rough case becomes worse than that in the smooth case.

Keywords: Natural convection; 3D random roughness; compressible flow; Nusselt number

1. Introduction

In modern industry, many facilities operate under conditions that involve high temperature differences, e.g., nuclear reactor cooling, and the cooling systems used in construction and solar collectors [1–3], so, in that case, the influence of compressibility of fluids on the heat transfer performance becomes conspicuous. On the other hand, to enhance the heat transfer, the roughness or the presence of obstacles on the surfaces from which heat transfer takes

place has been researched widely, but most studies only consider incompressible fluids [4–6]. Therefore, a study of the heat transfer considering both roughness and the compressibility of fluids is necessary and significant.

For the case of a high temperature difference (i.e., >30 K), Gray and Giorgini [7] recommended considering the compressibility of the fluid during numerical calculations, thus making it necessary to use a compressible flow solver because of the conspicuous density variations of fluids. However, when compared with the speed of sound, the magnitude of the fluid speed is too small to allow a compressible solver to be used directly. For this reason, Weiss and Smith [8] adopted a preconditioning method for application to natural convection in a horizontal annulus and their results showed that the accuracy of this method was satisfactory under the condition where the Rayleigh number was equal to 4.7×10^4. Yamamoto et al. [9] simulated natural convection in a horizontal circular pipe using the same method to deal with compressible flows at low velocities and proved that the preconditioning method could achieve good agreement with the experimental results in terms of the thermal boundary layers and the Nusselt number under the conditions of a temperature difference of 32.5 K and the Rayleigh number $Ra = 10^5$. In addition, the preconditioning method was shown to accelerate the simulation toward convergence under steady-state conditions [10].

Buoyancy driven flows in square cavities have previously been studied widely. Bajorek and Lloyd [11] used experimental methods to investigate the effects of rectangular partitions on the horizontal walls in a square cavity on the heat transfer between the two vertical walls. Their results showed that, when compared with a smooth cavity, the presence of the partitions caused the heat transfer to be reduced by 12% and 21% at high Grashof numbers and low Grashof numbers, respectively. Shakerin et al. [12] used experimental methods to study the heat transfer from hot walls with different numbers of rectangular roughness elements within a square enclosure. For a single roughness element, the mean Nusselt number along the hot wall showed an increase of 12% when compared with the smooth wall under the condition that the Rayleigh number was 10^6. However, there was an increment in the surface area of 32% when using the single roughness element in comparison with the smooth wall case. The mean Nusselt number of the case where two roughness elements were present showed a slight increase in

the mean Nusselt number (3.88% higher) when compared with the single roughness element case.

In addition to the rectangular roughness elements, sinusoidal roughness elements have also been studied recently by many researchers. Bhardwaj et al. [13] simulated the flow field in a porous right-angled triangular cavity with a sine-wave-shaped left wall and a smooth bottom wall to determine the effects of the fluctuating hot wall on the heat transfer and entropy generation properties of the cavity. Their results showed that, under the laminar flow condition, the undulation of the hot wall caused the strength of the vortex to be enhanced; in addition, both the average Nusselt number and the maximum Nusselt number were higher than in the zero-undulation case. The increment in the maximum Nusselt number was 53% for a Rayleigh number of 10^6 and a Darcy number of 0.01. However, in contrast, Yousaf and Usman [14] obtained a lower average Nusselt number along a hot wall with sinusoidal roughness elements. At an *Ra* of 10^6 and using 10 roughness elements, the average Nusselt number decreased by 12.25% when compared with that in the smooth wall case. Shahriari et al. [15] also observed a reduction in the Nusselt number. At $Ra = 10^5$, with eight sinusoidal roughness elements on both hot and cold walls in a square cavity, the Nusselt number decreased by approximately 20% when compared with that of the smooth wall case.

In most previous experimental or numerical researches, simple geometric shapes, such as thin sheets and rectangular or sinusoidal shapes, were selected as the shapes of roughness elements [12][14][15]. In contrast, to represent the roughness existing in nature, a three-dimensional artificial random roughness has been generated in the present study. The roughness elements are random in shapes and heterogeneous in sizes. Furthermore, by taking the working conditions of practical industrial applications into account, a compressible solver with an all-speed Roe scheme has been established as the appropriate numerical method to investigate buoyancy-driven flows.

Nomenclature

L_1, L_2, L_3	Width, Height and Depth of the square cavity
A	Area of sidewalls
C	Power spectral density (PSD)
d	Distance from the cell center to the closest geometry element
g	Gravitational acceleration
h	Height of individual roughness element
k	Theermal conductivity
Nu	Nusselt number
P	Pressure
Pr	Prandtl number
q	Wavevector
R	Gas constant
Ra	Rayleigh number based on cavity height, $g\beta_0 \Delta T {L_2}^3 Pr/{\nu_0}^2$
Rq	Root mean square roughness
T	Temperature
t	Physical time
u_1, u_2, u_3	Velocity components in x_1, x_2 and x_3 directions
x_1, x_2, x_3	Spatial coordinates

Greek symbols

β	Thermal expansion coefficient
ΔT	Temperature difference, $(T_H - T_C)$
$\Delta x_1, \Delta x_2, \Delta x_3$	Mesh size in x_1, x_2 and x_3 directions
Δt	Physical time step
$\Delta \tau$	Artificial time step
δ_{ij}	Kronecker delta
δ_{x_i}	Central difference operator
γ	Adiabatic index
Γ	Preconditioning matrix

θ	Nondimensional temperature, $(T - T_c)/(T_h - T_c)$
ρ	Density
τ	Artificial time
μ	Dynamic viscosity
ν	Kinematic viscosity
ϕ	Arbitrary physical value
Subscript	
C	Cold wall
H	Hot wall
IC	Interface cell
IP	Image point
l	Local value
overall	Average value over an entire sidewall
p	Primitive form of variables
w	Wall
0	Ambient or initial value
Superscript	
$*$	Nondimensional value
k	Artificial time
n	Physical time

2. Physical Model and Governing Equations

Because the three-dimensional geometries of random rough surfaces cannot be ignored in this work, the numerical simulations of the flows in the square cavity are performed under 3D conditions. Fig. 1 shows the physical model of current study with differentially heated vertical sidewalls and adiabatic top and bottom surfaces. A high temperature of T_H and a low temperature of T_C, which are both constant and isothermal, are set on the left and right sidewalls, respectively. The no-slip boundary condition is imposed on the top, bottom and both sidewalls of the cavities, but slip boundary condition is imposed on both x_3-direction boundaries

(at x_3/L_3 = 0 and x_3/L_3 = 1 planes). For all cavity flow, air with a Prandtl number (*Pr*) of 0.72 is selected as the working fluid. The initial temperature of the air contained in the core of the square cavity is $T_0 = (T_H + T_C)/2$ and the pressure is 101,300 Pa.

The artificial random surface roughness is generated based on a given power spectrum density [16][17], as illustrated in Fig. 2. In this research, the root mean square roughness (*Rq*) is equal to 1.5% of the cavity width (L_1), where $Rq = \sqrt{\frac{1}{n}\sum_{i=1}^{n} h_i^2}$, and h_i is the height of each roughness element from the mean plane of the roughness. On the mean plane's position, the heights of peaks and depths of valleys all add to zero. Because of the random distribution of the roughness elements, the depth-to-width aspect ratio (L_3/L_1) is selected to be 2 and the arrangement of the roughness elements is symmetrical with respect to the middle of the depth of the cavity. As noted above, in many previous works, the existence of the roughness will reduce the effective volume of fluid in the cavity. Therefore, to maintain a constant value for the effective volume, rough surfaces have been installed on both hot and cold sidewalls in this research, and the rough surface on the cold wall is generated by direct translation of the rough surface on the hot wall.

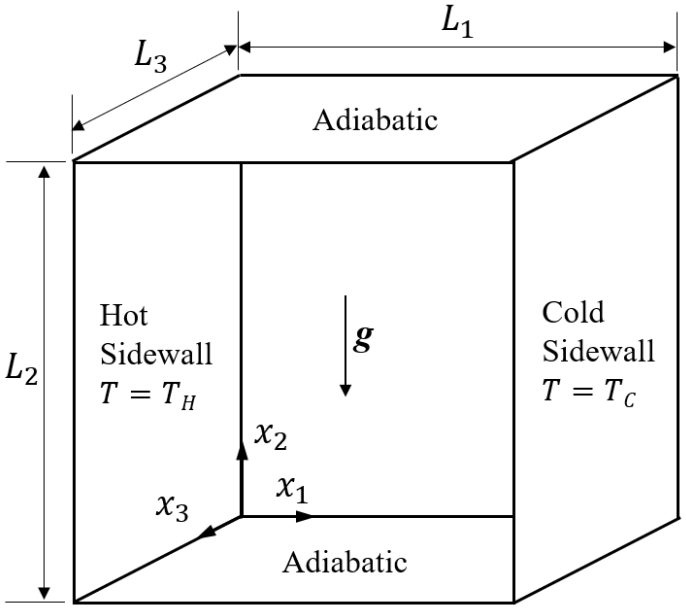

Figure 1. Simulation settings of the square cavity.

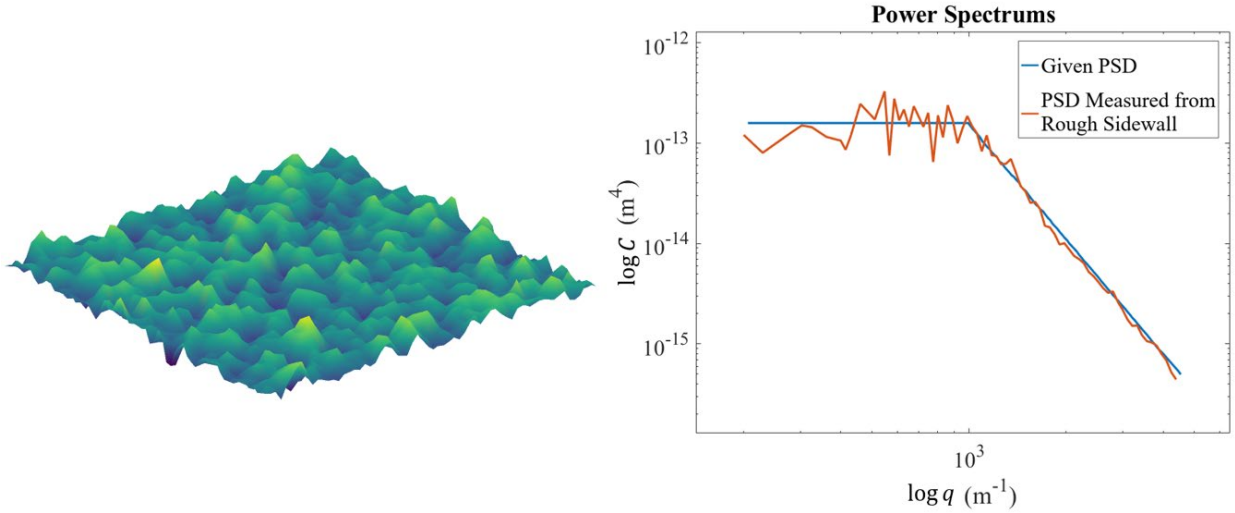

Figure 2. 3D random artificial roughness and the power spectrum.

To deal with the natural convection that occurs because of the buoyancy force, the following compressible governing equation has been considered:

$$\frac{\partial U}{\partial t}+\frac{\partial F_1}{\partial x_1}+\frac{\partial F_2}{\partial x_2}+\frac{\partial F_3}{\partial x_3}=S. \tag{1}$$

U and F_i can be written in following format:

$$U=\begin{bmatrix}\rho\\ \rho u_1\\ \rho u_2\\ \rho u_3\\ \rho e\end{bmatrix}, \tag{2}$$

$$F_i=\begin{bmatrix}\rho U_i\\ \rho u_i u_1+p\delta_{i1}-\mu A_{i1}\\ \rho u_i u_2+p\delta_{i2}-\mu A_{i2}\\ \rho u_i u_3+p\delta_{i3}-\mu A_{i3}\\ (\rho e+p)u_i-\mu A_{ij}u_j-k\frac{\partial T}{\partial x_i}\end{bmatrix}, \forall i,j=1,2,3, \tag{3}$$

and

$$S=\begin{bmatrix}0\\ 0\\ -(\rho-\rho_0)g\\ 0\\ -(\rho-\rho_0)gu_2\end{bmatrix}, \tag{4}$$

where $A_{ij} = \partial u_j/\partial x_i + \partial u_i/\partial x_j - 2/3(\nabla \cdot u)\delta_{ij}$ and δ_{ij} is the Kronecker delta. The relationship between the pressure and the density of the air is represented by the ideal gas equation, where $P = \rho RT$. According to Sutherland's Law [18], the viscosity (μ) and the thermal conductivity (k) of the working fluid are determined as follows:

$$\mu(T) = \mu_0 (\frac{T}{T_0})^{\frac{3}{2}} \frac{T_0+110.4}{T+110.4}, \quad (5)$$

$$k(T) = \frac{\mu(T)\gamma R}{(\gamma-1)Pr}, \quad (6)$$

where $\rho_0 = 1.18\ kg/m^3$, $g = 9.81\ m/s^2$, $\mu_0 = 1.85 \times 10^{-5}\ N \cdot s/m^2$, $T_0 = 298.06\ K$, $\gamma = 1.4$, $R = 287\ J/kg$, and $Pr = 0.72$.

3. Numerical Method

3.1 Compressible solver

In natural convection, the magnitude of the fluid velocity due to the buoyancy force is generally smaller than the speed of sound by several orders of magnitude. For this reason, the original compressible solvers are unsuited to analysis of this type of flow field. To increase the efficiency for solution of natural convection problems involving compressible flows, a preconditioning method is used to resolve the governing equations, which is developed by Weiss and Smith [8]. When combined with the Roe scheme [19] and the dual time-stepping method [20], the new governing equation is shown as follows:

$$\Gamma \frac{\partial U_p}{\partial \tau} + \frac{\partial U}{\partial t} + \frac{\partial F_1}{\partial x_1} + \frac{\partial F_2}{\partial x_2} + \frac{\partial F_3}{\partial x_3} = S, \quad (7)$$

where Γ is the preconditioning matrix provided by Weiss and Smith, U_p is the primitive form of the variables $[P, u_1, u_2, u_3, T]$, and U is the conservative form of $[\rho, \rho u_1, \rho u_2, \rho u_3, \rho e]$. τ and t represent the artificial and physical times, respectively.

The discretized form of Eq. (7) is

$$\Gamma\frac{U_p^{k+1}-U_p^k}{\Delta\tau}+\frac{3U^{k+1}-4U^n+U^{n-1}}{2\Delta t}+\frac{1}{\Delta x_1}\left(F1_{i+1/2,j,k}^{k+1}-F1_{i-1/2,j,k}^{k+1}\right)+\frac{1}{\Delta x_2}\left(F2_{i,j+1/2,k}^{k+1}-F1_{i,j-1/2,k}^{k+1}\right)+$$
$$\frac{1}{\Delta x_3}\left(F3_{i,j,k+1/2}^{k+1}-F3_{i,j,k-1/2}^{k+1}\right)=S^k. \quad (8)$$

The iterations of the artificial time and the physical time are indicated by the superscripts k and n shown in Eq. (8). It should be noted that when the iteration of the artificial time reaches convergence, the residual of $\partial U_p/\partial\tau$ is less than 10^{-3}, and the magnitude of the artificial term at the (k+1)th step is equivalent to the magnitude of the physical time term at the (n+1)th step, then Eq. (8) would then return approximately to the original Navier-Stokes equation.

Eq. (8) can be expressed in the following format as:

$$\left[\frac{I}{\Delta\tau}+\Gamma^{-1}M\frac{3}{2\Delta t}+\Gamma^{-1}(\delta_{x_1}A_p^k+\delta_{x_2}B_p^k+\delta_{x_3}C_p^k)\right]\Delta U_p=\Gamma^{-1}R^k, \quad (9)$$

where $M=\partial U/\partial U_p$, $A_p=\partial F_1^k/\partial U_p$, $R^k=S^k-(3U^k-4U^n+U^{n-1})/2\Delta t-(\delta_{x_1}F_1^k+\delta_{x_2}F_2^k+\delta_{x_3}F_3^k)$, and δ_{x_i} is the central difference operator. Xu et al. [21] recommended setting the pseudo-time step, $\Delta\tau$, to infinity then the Newton linearization error will be zero in each physical time step. Eventually, Eq. (9) can be rewritten into Eq(10):

$$\left[\Gamma^{-1}M\frac{3}{2\Delta t}+\Gamma^{-1}(\delta_{x_1}A_p^k+\delta_{x_2}B_p^k+\delta_{x_3}C_p^k)\right]\Delta U_p=\Gamma^{-1}R^k, \quad (10)$$

The lower-upper symmetric-Gauss-Seidel (LUSGS) implicit method is then used to solve Eq. (10).

It is helpful to divide the flux term given in Eq. (3) into an inviscid term and a viscid term, as shown in Eq. (11) and Eq. (12), respectively, to perform the calculation of R^k in Eq. (10). The inviscid term in Eq. (11) can then be discretized into Eq. (13) using the Roe scheme.

$$F_{inviscid}=\begin{pmatrix}\rho u_i\\ \rho u_iu_1+p\delta_{i1}\\ \rho u_iu_2+p\delta_{i2}\\ \rho u_iu_3+p\delta_{i3}\\ (\rho e+p)u_i\end{pmatrix}, \quad (11)$$

$$F_{viscous}=-\begin{pmatrix}0\\ \mu A_{i1}\\ \mu A_{i2}\\ \mu A_{i3}\\ \mu A_{ij}u_j+\lambda\frac{\partial T}{\partial x_i}\end{pmatrix}, \quad (12)$$

$$F_{inviscid,i+1/2} = \frac{1}{2}[F_R(U) + F_L(U)] + F_d, \quad (13)$$

where F_d is the Roe dissipation term.

For the two convective terms (F_R and F_L) shown in Eq. (13), the values at the cell interfaces are calculated by interpolation of the corresponding values from a group of cell centers through a fifth-order MUSCL approach [22] without limiter functions, which are shown in the following way:

$$U_{L_{1+1/2}} = \frac{1}{60}[-3U_{i+2} + 27U_{i+1} + 47U_i - 13U_{i-1} + 2U_{i-2}], \quad (14)$$

$$U_{R_{1+1/2}} = \frac{1}{60}[2U_{i+3} - 13U_{i+2} + 47U_{i+1} + 27U_i - 3U_{i+1}]. \quad (15)$$

3.2 Immersed boundary method for compressible flows

Because of the complex geometry of the random rough surface, the immersed boundary method(IBM) has been applied [23] to ensure that the geometrical details are reproduced as accurately as possible. The key point of IBM is to simulate the existence of geometry by imposing the physical values into the numerical grids in the vicinity of geometry. Figure 3 shows the configuration of IBM. The cells which are defined as interface cell (IC) has the characteristic that the distance (*d*) from the cell center to the closest geometry element is less than one cell size. Image point (IP) is the point that the distance from which to IC is equal to *d* in the normal direction of the geometry element. IC and IP must be on the same side of geometry. Then, according to the relative locations of surrounding cells to IP, the physical value at IP, ϕ_{IP}, can be calculated by bilinear interpolation:

$$\phi_{IP} = w_1\phi_1 + w_2\phi_2 + w_3\phi_3 + w_{IC}\phi_{IC}, \quad (16)$$

where w_1, w_2, w_3 and w_{IP} can be obtained using VanderMonde matrix [23]. Tullio et al.[24] recommended applying linear interpolation to evaluate ϕ_{IC}, shown in the following equations:

$$\phi_w = \phi_{IC} - \left(\frac{\partial\phi}{\partial n}\right)d = \phi_{IC} - \frac{\phi_{IP}-\phi_w}{2d}d, \quad (17)$$

$$\phi_{IC} = \frac{1}{2}(\phi_w + \phi_{IP}), \tag{18}$$

In present study, the no-slip and isothermal conditions are implemented on the walls, so ϕ_w is an assigned value ϕ_{assign}, thus the Dirichlet condition should be considered. Then according to equations (16), (17) and (18), ϕ_{IC} can be presented as follows:

$$\phi_{IC} = \frac{w_1\phi_1 + w_2\phi_2 + w_3\phi_3 + \phi_{assign}}{2 - w_{IC}} \text{ Dirichlet condition,} \tag{19}$$

However, for pressure, Neumann condition, which considers $\phi_w = \phi_{IP}$, should be used, then ϕ_{IC} can be presented as follows:

$$\phi_{IC} = \frac{w_1\phi_1 + w_2\phi_2 + w_3\phi_3}{1 - w_{IC} + \varepsilon} \text{ Neumann condition,} \tag{20}$$

where ε is a small value to prevent the denominator becoming zero. Because when IC is very close to the wall, w_{IC} will approach 1.

In authors' previous study [25], the natural convection of a heated sphere has been simulated through the IBM mentioned above. The comparison of the averaged *Nu* shows good agreement with the result of Jia and Gogos[26], and the error is only 0.343%.

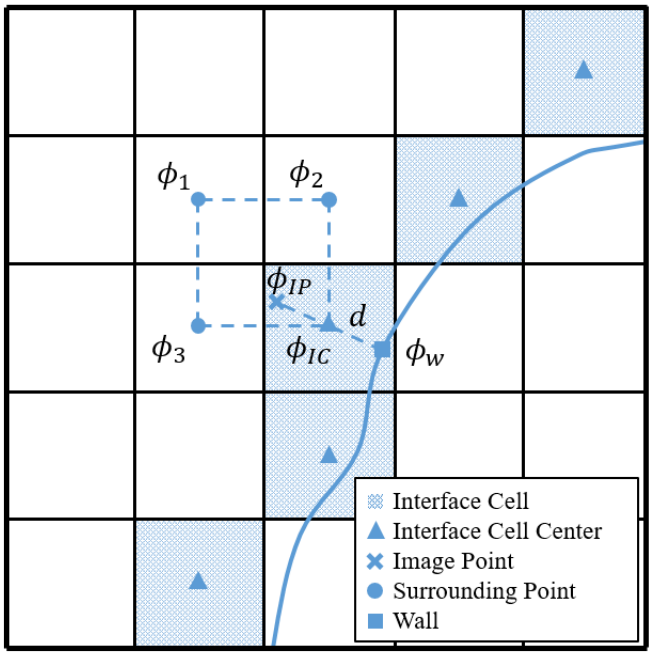

3.3 Building cube method

The building cube method (BCM) is used to provide higher computation efficiency and better load balancing on a massively parallel computing system [25]. The BCM divides the calculation domain into several cubes, and each cube contents 16^3 meshes. In any individual cube, the mesh spacings along the three orthogonal axes (directions x_1, x_2, and x_3) are same, which allows the details of the flow fields between two roughness elements to be captured more easily.

4. Results and Discussion

4.1 Investigation of fluid compressibility in enclosed square cavity

To discuss the effects of the compressible fluid on heat transfer, 3D cavities, shown in Fig. 1, with smooth hot and cold sidewalls are investigated in this section. For all cavities, the Rayleigh number remains constant, where the Rayleigh number $Ra = g\beta_0 \Delta T {L_2}^3 Pr/{\nu_0}^2 = 10^6$ and all fluid properties are determined based on the ambient temperature.

With regard to the influence of the compressibility of the working fluid on the heat transfer, three different temperature differences (10 K, 50 K, and 120 K) have been studied and the mesh distributions have been shown in Figure 4 (a). The finest grids are implemented in the vicinity of two sidewalls, and to save the computational resources, the coarser grids are implemented in the core regions of the cavities. There are 256 finest grids along with the height (L_2) direction of the enclosed cavities, and the distributions of grids along the depth (L_3) direction are uniform for all three cases. The Courant number (*CFL*) for all cases is set as 0.5 where $CFL = \max(u_i \cdot \Delta t/\Delta x_i), i = 1, 2, 3$ to represent the components acting along the three axes in the coordinate system.

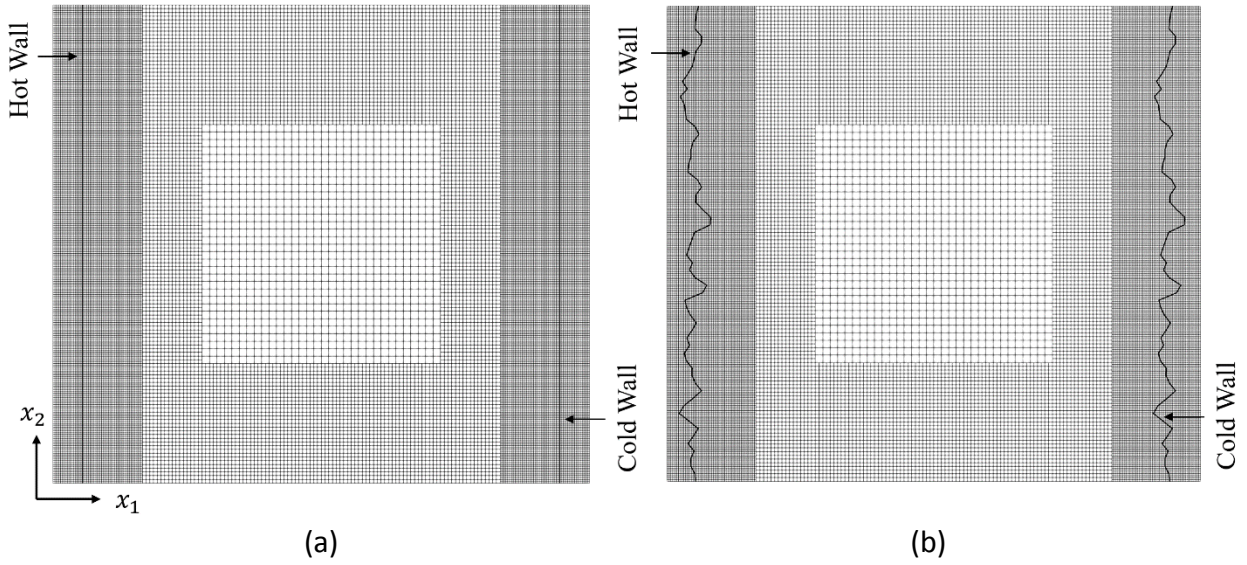

(a) (b)

Figure 4. Numerical grids distributions of smooth (a) and rough (b) cases at x_3 = 0.5 plane

Table 1 shows the average Nusselt numbers across the x_2-direction and the maximum values of the local Nusselt numbers on the hot sidewalls across the height at $x_3/L_3 = 0.5$ plane; these numbers can be obtained using Eqs. (21) and (22). The average Nusselt number over entire hot sidewall is calculated through Eq. (23). The maximum nondimensional vertical velocity at the center of the hot sidewall across the nondimensional width of the cavity (x_1/L_1) is also presented in the table. The nondimensional velocity is defined as $u_i^* = u_i/\sqrt{g\beta_0 \Delta T L_2}$.

$$\overline{Nu} = \frac{1}{L_2}\int_0^{L_2} Nu_l dx_2, \tag{21}$$

$$Nu_l = \frac{L_2}{k_0(T_h - T_c)} k(T) \frac{\partial T}{\partial x_1}, \tag{22}$$

$$\overline{Nu}_{overall} = \frac{1}{A}\int_0^A Nu_l dA, \tag{23}$$

where $k_0 = k(T_0)$ and $A = L_2 \cdot L_3$.

Table 1. Convergence behaviors of hydrodynamic quantities and Nusselt numbers.

Ra	Ref.	Numerical method	$u_2^*{}_{\max}$ (x_1/L_1)	$\overline{Nu}$
10^6	E Tric[27]	Incompressible	0.258 (0.033)	8.877
	A Xu[28]	Incompressible	0.258 (0.037)	8.881
	Present	Compressible (10 K)	0.260 (0.039)	8.854
	Present	Compressible (50 K)	0.259 (0.041)	8.874
	Present	Compressible (120 K)	0.264 (0.043)	8.787

The average Nusselt numbers of the three cases with various temperature differences from Table 1 show good agreement with the results from previous studies at the *Ra* of 10^6. The maximum deviation is 1.06%, which is the error between the case with the temperature difference of 120 K and the results of A Xu [28]. Fig. 5 presents the local Nusselt number distributions at the middle depth on the hot sidewall. For the compressible solver, it is evident that as ΔT increases, the pattern of the local *Nu* numbers on the hot wall becomes steeper, i.e., the maximum value of the local *Nu* increases, but the cases with larger ΔT values will have smaller local *Nu* magnitudes in the $x_2/L_2 > 0.3$ region. Between the case with the temperature difference of 120 K and the results of Kuyper et al. [29], the maximum local Nusselt numbers

reach their largest deviation of 6.233%. For the vertical velocity, Table 1 indicates that as the temperature difference increases, the location of the maximum vertical velocity moves away from the hot sidewalls. This phenomenon where the distribution of the local Nusselt number changes with the temperature difference was also reported in [30] and it was attributed to the temperature dependences of the fluid properties, as shown in Eq. (5) and Eq. (6). In summary, a temperature difference between two heated sidewalls will change the local Nusselt number distribution but will have no effect on the average Nusselt number for a Rayleigh number of 10^6. Therefore, it becomes necessary to consider adopting a compressible solver when local region heat transfer is the research target.

4.2 Grid sensitivity for the enclosure with rough sidewalls

Due to the complex 3D random roughness, the Immersed-boundary method which is mentioned in section 3.2 requires suitable girds to capture the geometric features of the roughness. Meanwhile, for the simulation of the fluid among the roughness elements, an appropriate mesh resolution is necessary. Therefore, in this part, the cavity with rough sidewalls is filled by numerical grids with 3 different resolutions shown in Table 2. The mesh resolutions of 128 and 512 are respectively generated by coarsening or refining the grids based on the resolution of 256, shown in Fig. 4 (b). For convenience, we use grid 128, grid 256 and grid 512 to represent these three mesh resolutions. Table 2 shows the average Nusselt numbers over the entire hot sidewall from these 3 different grid strategies. After a comparison between the results of grid 256 and grid 512, the average Nusselt numbers are almost same and the difference is only 0.023%. However, the difference between grid 512 and grid 128 is 10.942%.

Further, Figure 6 shows the nondimensional temperature distributions across the horizontal centerline of the cavities' midplane (x_2/L_2 = 0.5 line at x_3/L_3 = 0.5 plane). The profiles show that the temperature distributions of grid 256 and gird 512 almost overlapped near the hot sidewall, but due to the insufficient resolution, grid 128 shows a different profile of temperature from the other two mesh resolutions. According to the arrangement of roughness elements in

current study, for the resolution of grid 256, there are at least 4 grids for one peak or one valley on the rough surface, but for the resolution of grid 128, this number is only 2 for one peak or one valley.

Thus, all subsequent results in the following section are based on the mesh resolution of grid 256.

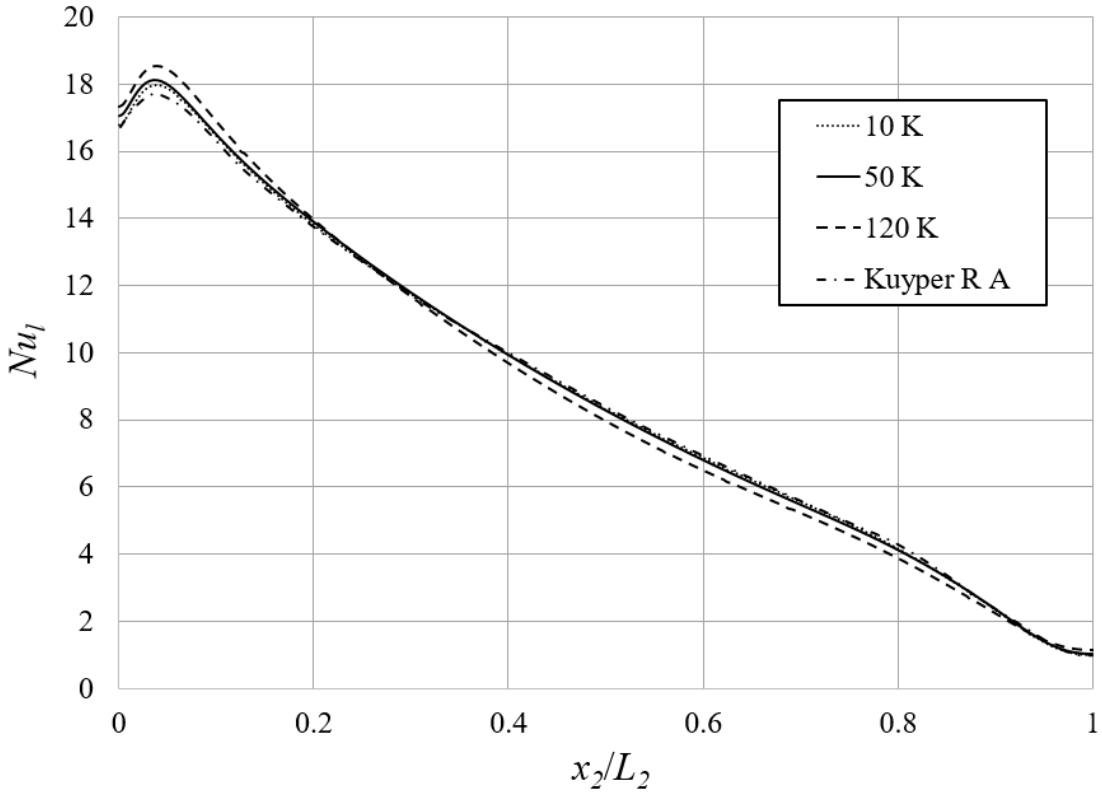

Figure 5. Local Nusselt numbers of smooth cases with various temperature differences.

Table 2. Values of average *Nu* for grid sensitivity study

Mesh resolution	$\overline{Nu}_{overall}$	Difference (%)
512	8.719	-
256	8.717	0.023
128	7.765	10.942

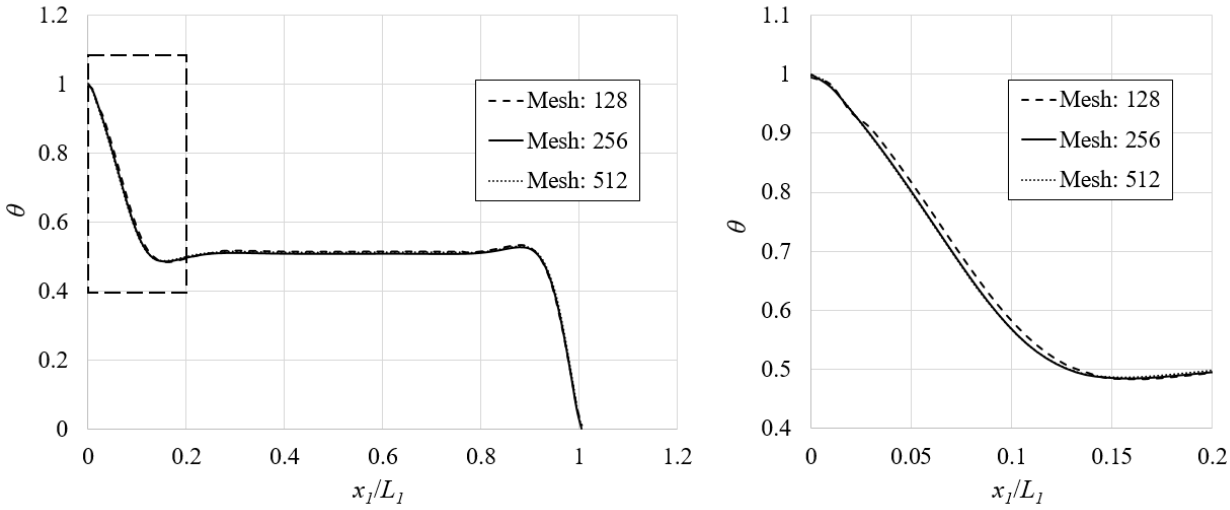

Figure 6. Nondimensional temperature profiles

4.3 Influence of roughness on heat transfer

Figure 7 shows the local Nusselt number distributions on the hot sidewalls of the smooth and rough cavity cases. For both the smooth case and the rough case, the local Nusselt numbers show a trend of being higher in the upstream region and lower in the downstream region. Because of the existence of the peaks and valleys on the sidewalls, the local Nusselt number distribution on the rough surface shows good agreement with the distribution of the roughness elements and the local Nusselt numbers on the peaks are larger than those in the valleys. Table 3 shows the average Nusselt numbers over the entire hot sidewall and the maximum values of the local Nusselt numbers for the two cases, where the symbols of + and – represent that compared with the results of the smooth case, the increase or decrease of the investigated values due to the rough sidewalls respectively. In Table 3, the largest local Nusselt number in the rough cavity case is much larger than that in the smooth case; however, in contrast, the average Nusselt number of the rough case is slightly smaller than that in the smooth case by 1.769%.

Table 4 presents the local average Nusselt numbers of the two cases above in the upstream and downstream regions. Here, the local average Nusselt number is considered to be the integral of the Nusselt number on a local part of the heated sidewall, as defined in Eq. (24):

$$\overline{Nu}_l = \frac{1}{A_l}\int_0^{A_l} Nu_l dA, \tag{24}$$

where the subscript *l* indicates a specific local part of the heated sidewall.

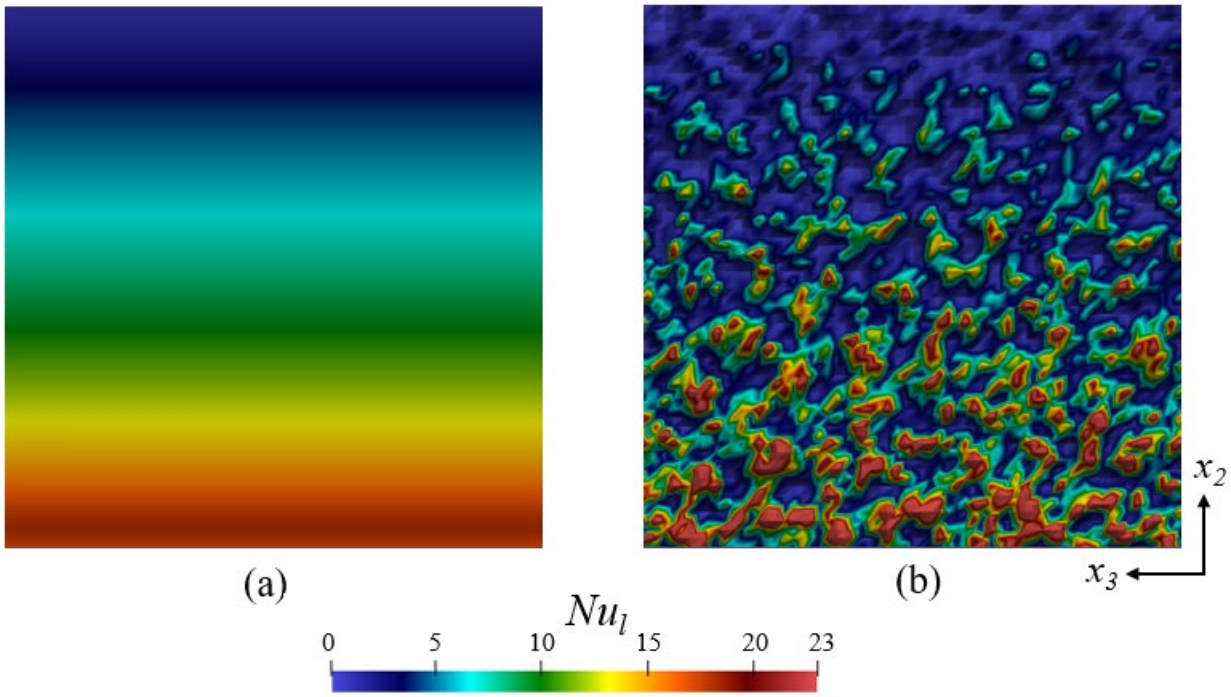

Figure 7. Distributions of the local *Nu* values of the (a) smooth and (b) rough cases on the hot walls.

Table 3. Maximum values of the local Nusselt numbers and the average Nusselt numbers for the smooth and rough cases.

	smooth	rough	Difference (%)
Nu_{lmax}	18.134	60.207	+232.012
$\overline{Nu}_{overall}$	8.874	8.717	-1.769

Table 4. Local average Nusselt numbers in the upstream and downstream regions.

	Smooth	Rough	Difference (%)
Upstream (x_2/L_2 = 0 to 0.1)	17.613	18.622	+5.729
Downstream (x_2/L_2 = 0.75 to 1)	2.822	2.743	-2.799

When compared with the smooth case, the local average Nusselt number in the upstream region in the rough case is higher, but in the downstream region, the local average Nusselt number in the rough case is smaller than that in the smooth case. To explain this phenomenon in greater depth, the temperature distribution on a slice at a quarter of the depth of the cavity is shown in Fig. 8, where the nondimensional temperature is calculated using the following equation: $\theta = (T - T_c)/(T_h - T_c)$. In the upstream region, the peaks will reduce the thermal boundary layer thickness, while the valleys can make the thermal boundary layer thicker, which means that the thermal boundary layer will undergo drastic changes in thickness within this region. However, as the thermal boundary layer develops, the thickness will inevitably increase, and then the effects of the roughness elements on the thermal boundary layer will decrease. From Fig. 8 (c) and (d), the isothermal surfaces are distorted by the roughness elements near the rough sidewall, but in the core region of the cavities, the temperature stratifications are almost identical for smooth and rough cases.

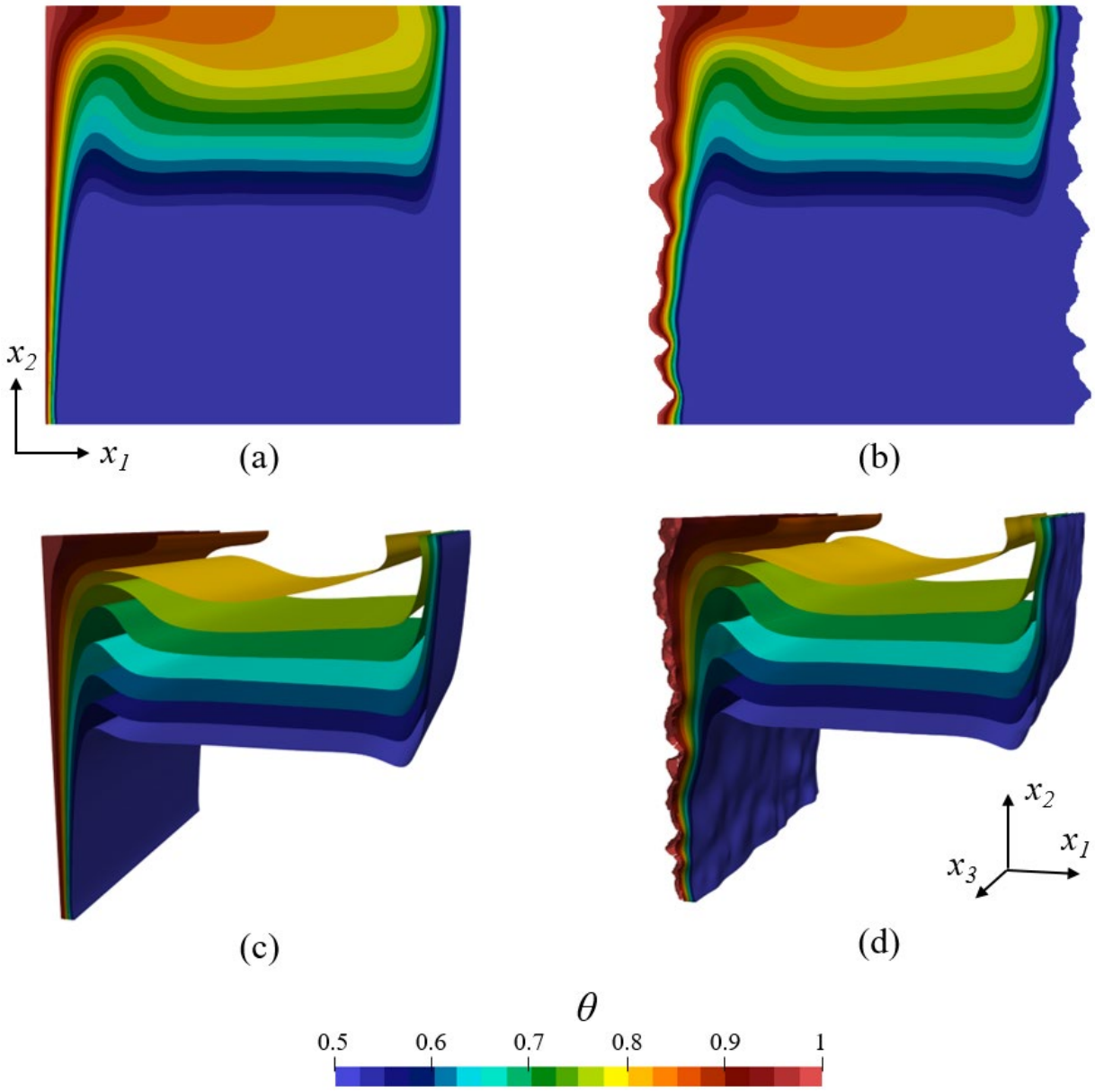

Figure 8. Temperature distributions of smooth and rough cases: (a, b) slices at x_3/L_3=0.25 plane (c, d) isothermal surface in half cavity from x_3/L_3=0 to 0.5.

Fig. 9 (a) and (b) show the nondimensional velocity magnitudes of the two cases on three different planes (x_1/L_1 = 0.005, x_2/L_2 = 0.5 and x_3/L_3 = 0.25) respectively. From this figure, when

the flow approaches the peaks on the rough surface, there is a slight acceleration in the magnitude of the velocity when compared with the smooth case, but after the peak has been crossed, the ensuing valley will cause the fluid velocity to decelerate sharply. Unlike the influence of the rough surface on the thermal boundary layer, the influence of the rough surface on the magnitude of the velocity in the downstream region is obvious. This can therefore be considered to be one explanation as to why the local Nusselt number distribution presents the tendency where, in the case with the rough heated sidewalls, the local Nusselt number is higher than that in the smooth case in the vicinity of the peaks in the upstream region, while in the downstream region, the local average Nusselt number is smaller than that in the smooth case.

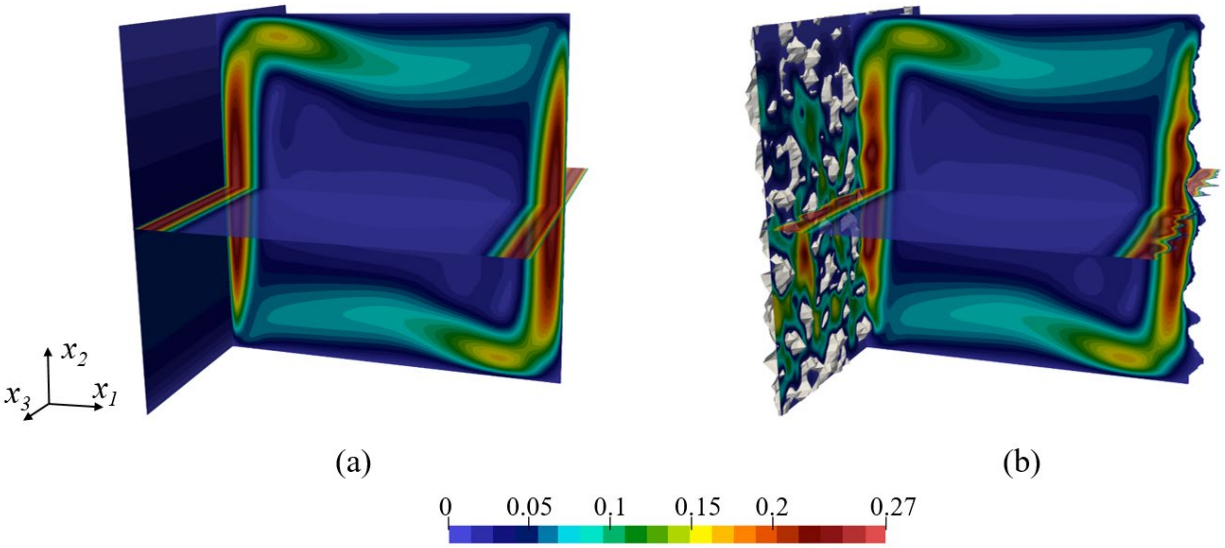

Figure 9. Nondimensional velocity magnitudes (where (a) and (b) show the smooth and rough cases, respectively) and vectors (where (c) and (d) show the smooth and rough cases, respectively).

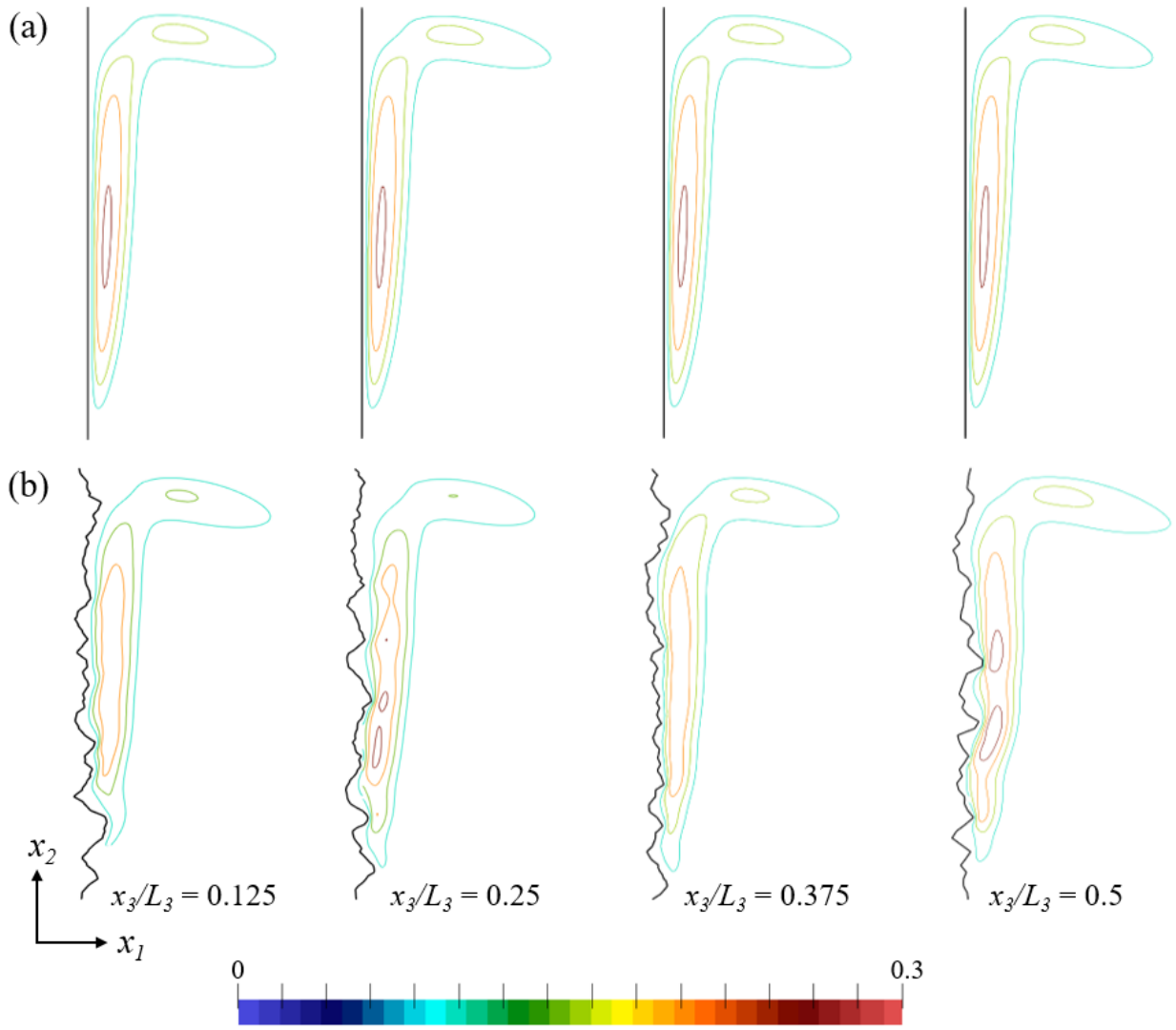

Figure 10. Contours of Nondimensional velocity magnitude of smooth (a) and rough (b) cases at different x_1-x_2 planes

Figure 10 shows the contours of the nondimensional velocity magnitude of both smooth and rough cases near the hot sidewall at four different x_1-x_2 planes (x_3/L_3 = 0.125, 0.25, 0.375 and 0.5), where the black curves are the profiles of hot sidewalls at these planes. From the figure, the velocity magnitudes of the flow field in the vicinity of the rough wall are smaller than smooth case generally, and only part of the fluid will be accelerated due to the roughness. In

the region where the shape of roughness elements does not change drastically, the roughness plays a role more in slowing down the velocity of adjacent fluid rather than accelerating it.

Fig. 11 (a) and (b) show the velocity vector fields in the half region located close to the hot sidewall at the same location used in Fig. 10 (a) and (b). The figure containing the velocity vectors shows no evident fluid circulation to be found in the area between the two roughness elements on the x_1-x_2 plane at $Ra = 10^6$. In addition, the eddies that occur near the core regions of the two cavities do not show particularly notable differences.

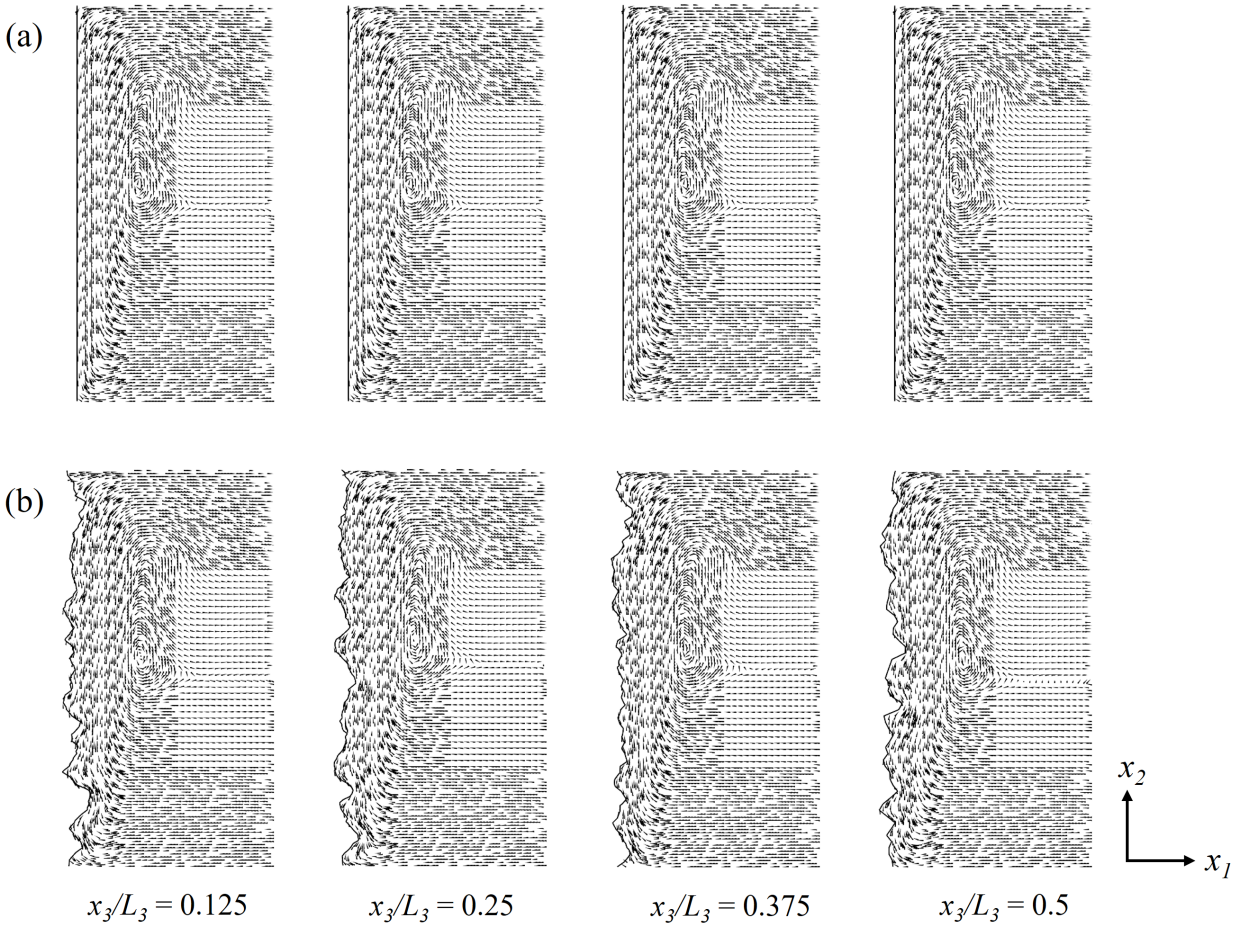

Figure 11. Velocity vector fields of smooth (a) and rough (b) cases at different x_1-x_2 planes

In Fig. 12, the components of the nondimensional temperature gradients in the x_1-direction have been measured in the cavities with both rough and smooth sidewalls at two measurement locations. These two locations are two different lines parallel to the x_2-direction($x_3/L_3 = 0.55$ line and $x_3/L_3 = 0.8$ line) at $x_1/L_1 = 0.05$ plane starting from the mean plane of the hot rough sidewall. The black curves shown in Fig. 12 are the profiles of the hot rough surfaces at x_1-x_2 planes where two measurement locations lie respectively. The figure shows that in the upstream regions, the temperature gradient fluctuates dramatically and this trend follows the distribution of the roughness elements perfectly, which means that higher peaks will bring increased heat transfer. However, this dominance of the roughness decreases in the end region, particularly in the downstream region, and after the nondimensional height exceeds 0.8, the patterns from the two cases almost overlap. In Fig. 13, at the center of the adiabatic surface and across the heights of the cavities, the temperatures in both the rough and smooth cases have been measured. The temperature curves show very good agreement, thus indicating that the random artificial roughness cannot influence the heat transfer that occurs in the core region of the square cavity.

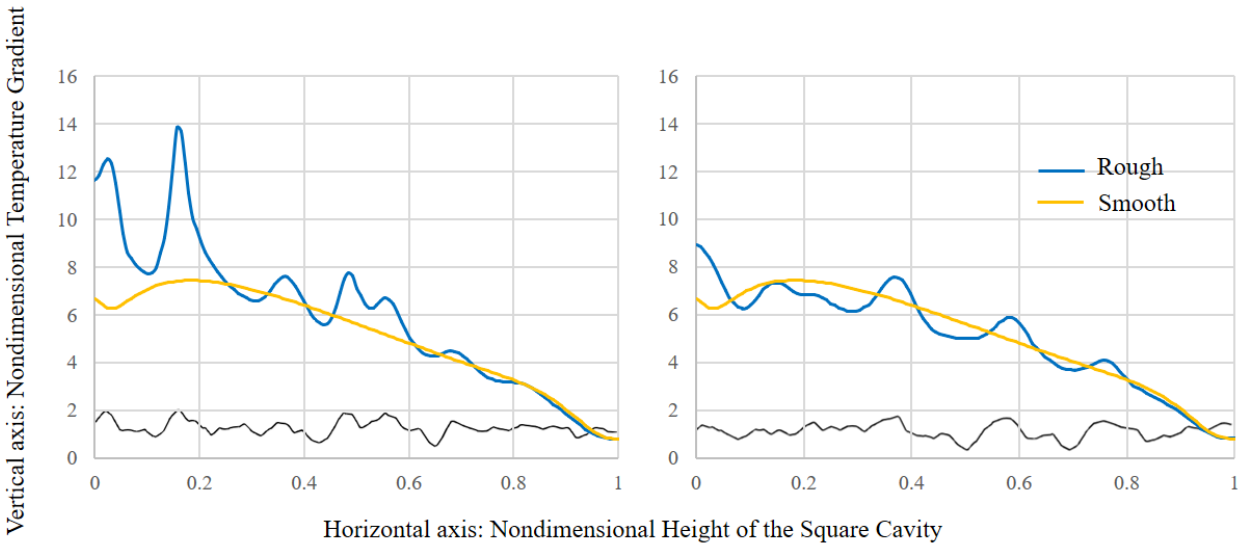

Figure 12. Nondimensional temperature gradients across the height of the cavity at two different measurement locations (black curves: profiles of the rough surface at the two measurement locations).

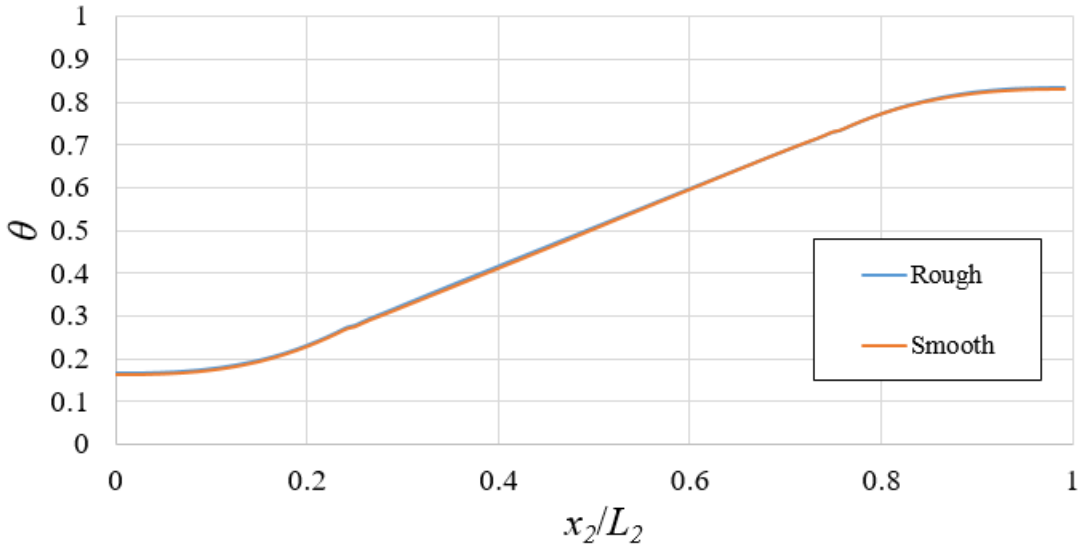

Figure 13. Nondimensional temperatures at the center of the adiabatic surface across the cavity height.

Figure 14 and Fig. 15 show the effects of the surface roughness on the velocity component in the x_3-direction. The slices in Fig. 14 are located at different x_1-x_2 planes. The magnitudes of this

velocity component shows a trend where the initial magnitude is very small in the upstream region and then increases to reach a maximum in the middle region; however, in the downstream region, deceleration occurs. Furthermore, the effect of the rough surface cannot reach the core region of the cavity. The slice shown in Fig. 15 is located at a position of 0.5% of the cavity width from the mean plane of the rough surface. In this figure, the changes in the colors near the roughness elements and the speed vectors demonstrate that the geometry of the 3D random roughness structure gives the fluid the possibility of bypassing the roughness elements and no evident eddies were found. However, in two-dimensional cavity flow with homogeneous roughness elements on the cavity sidewalls [15][16], the fluid will become trapped more easily between two adjacent roughness elements, and this represents a major cause of the reduction in the heat transfer.

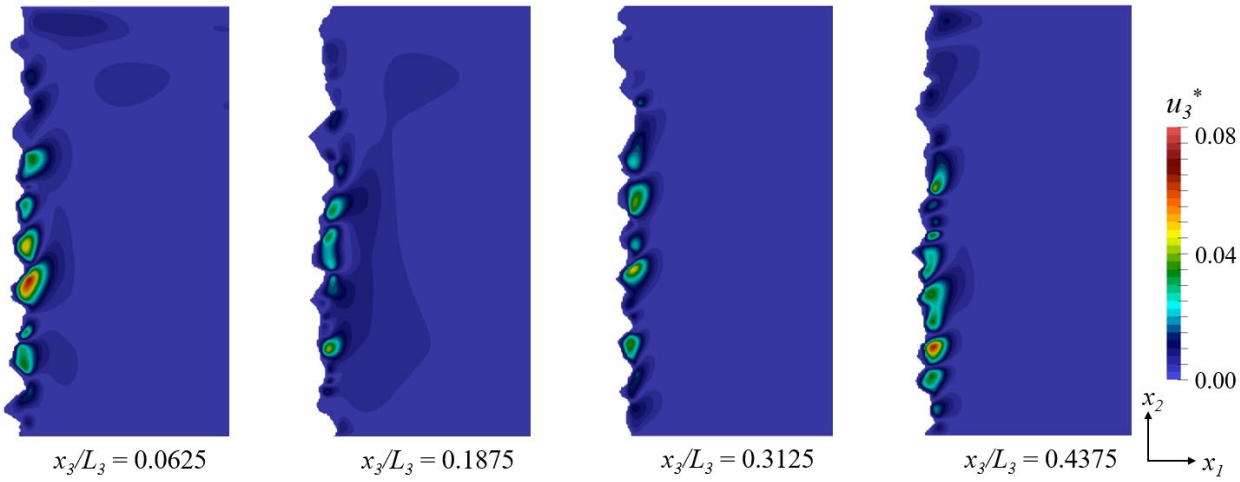

Figure 14. Magnitudes of the velocity component in the x_3 direction.

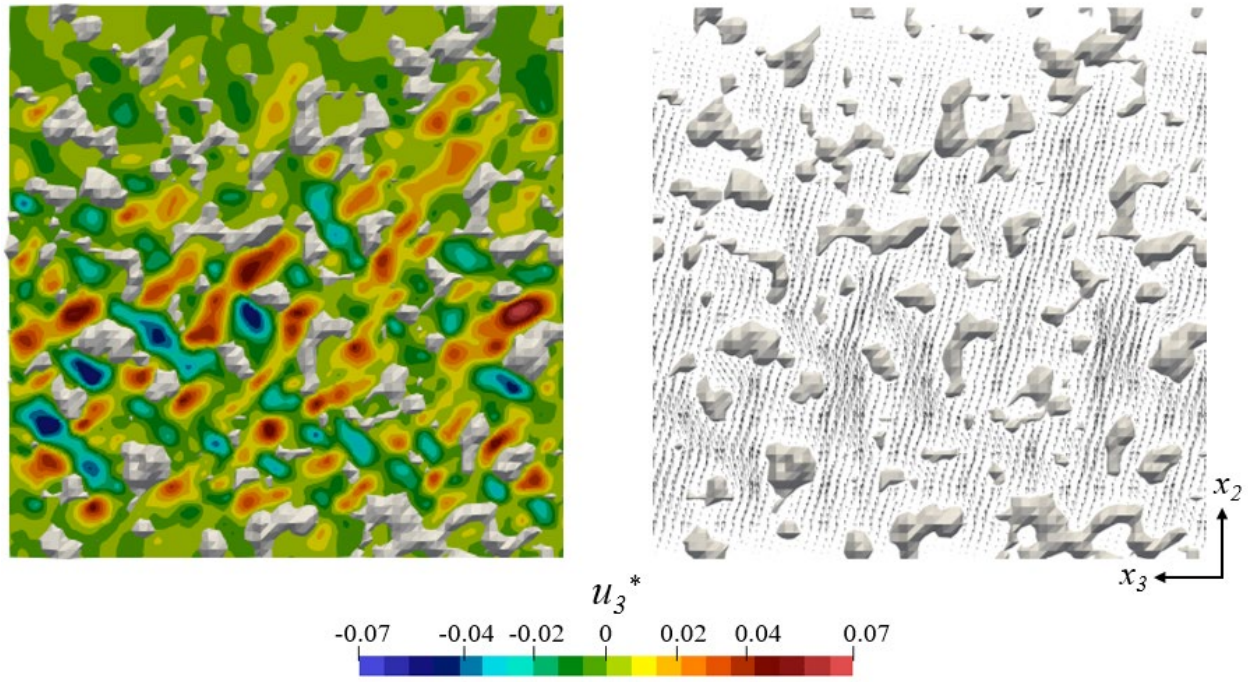

Figure 15. Flow field among the roughness elements of the hot sidewall.

5. Conclusions

Natural convection in a cavity with 3D random roughness elements on its sidewalls has been investigated at a Rayleigh number of 10^6 using a compressible solver. The roughness was generated using a given power spectrum density and the temperature difference between the two sidewalls was 50 K. The distribution of the local Nusselt number on the hot sidewall showed that cavities with both rough and smooth sidewalls followed a trend where the local Nusselt number was higher in the upstream region and lower in the downstream region. The maximum value of the local Nusselt number for the rough surface is 2.32 times larger than that in the smooth case, but the average Nusselt number is 1.8% smaller than that in the smooth case. The peaks on the rough surface will reduce the thermal boundary layer thickness but the corresponding valleys will increase this thickness in the upstream region. However, in the downstream region, the thermal boundary layer thickness is thick enough to ensure that this effect is no longer obvious. Near the hot sidewall, the peaks accelerate the flow field slightly, but the valleys cause a conspicuous deceleration of the flow field; this phenomenon exists in

both the upstream and downstream regions. Therefore, the Nusselt number on the rough surface in the upstream region shows a larger average value than that of the smooth case in the same region, but will show a smaller average value in the downstream region. However, the fluid will bypass the elements in the 3D simulations, rather than become trapped between two roughness elements, and this is one reason why the average Nusselt number in the rough case is not much smaller than that in the smooth case.

Acknowledgements

Funding: This work was supported by Japan Society for the Promotion of Science (JSPS) KAKENHI [Grant number JP19K14890].

References

[1] I. Amber, T.S. O'Donovan, Natural convection induced by the absorption of solar radiation: A review [J], Renewable and Sustainable Energy Reviews 82 (2018) 3526–3545.

[2] Y. Ma, Z. Yang, Simplified and highly stable thermal Lattice Boltzmann method simulation of hybrid nanofluid thermal convection at high Rayleigh numbers [J], Physics of Fluids 32 (1) (2020) 012009.

[3] M.R. Amin, Natural convection heat transfer in enclosures fitted with a periodic array of hot roughness elements at the bottom [J], International Journal of Heat and Mass Transfer 36 (3) (1993) 755–763.

[4] X. Zhu, R.J.A.M. Stevens, R. Verzicco, et al., Roughness-facilitated local 1/2 scaling does not imply the onset of the ultimate regime of thermal convection [J], Physical Review Letters 119 (15) (2017) 154501.

[5] S. Wagner, O. Shishkina, Heat flux enhancement by regular surface roughness in turbulent thermal convection [J], Journal of Fluid Mechanics, 763 (2015) 109.

[6] B.N. Prasad, J.S. Saini, Effect of artificial roughness on heat transfer and friction factor in a solar air heater [J], Solar Energy 41 (6) (1988) 555–560.

[7] D.D. Gray, A. Giorgini, The validity of the Boussinesq approximation for liquids and gases [J], International Journal of Heat and Mass Transfer 19 (5) (1976) 545–551.

[8] J.M. Weiss, W.A. Smith, Preconditioning applied to variable and constant density flows [J], AIAA Journal 33 (11) (1995) 2050–2057.

[9] S. Yamamoto, D. Niiyam, B.R. Shin, A numerical method for natural convection and heat conduction around and in a horizontal circular pipe [J], International Journal of Heat and Mass Transfer 47 (26) (2004) 5781–5792.

[10] E. Turkel, Preconditioning techniques in computational fluid dynamics [J], Annual Review of Fluid Mechanics 31 (1) (1999) 385–416.

[11] S.M. Bajorek, J.R. Lloyd, Experimental investigation of natural convection in partitioned enclosures [J], Journal of Heat Transfer 104 (3) (1982) 527–532.

[12] S. Shakerin, M. Bohn, R.I. Loehrke, Natural convection in an enclosure with discrete roughness elements on a vertical heated wall [J], International Journal of Heat and Mass Transfer 31 (7) (1988) 1423–1430.

[13] S. Bhardwaj, A. Dalal, S. Pati, Influence of wavy wall and non-uniform heating on natural convection heat transfer and entropy generation inside porous complex enclosure [J], Energy 79 (2015) 467–481.

[14] M. Yousaf, S. Usman, Natural convection heat transfer in a square cavity with sinusoidal roughness elements [J], International Journal of Heat and Mass Transfer 90 (2015) 180–190.

[15] A Shahriari, E.J. Javaran, M. Rahnama, Effect of nanoparticles Brownian motion and uniform sinusoidal roughness elements on natural convection in an enclosure [J], Journal of Thermal Analysis and Calorimetry 131 (3) (2018) 2865–2884.

[16] M.M. Kanafi, A.J. Tuononen, Top topography surface roughness power spectrum for pavement friction evaluation [J], Tribology International 107 (2017) 240–249.

[17] Y. Xian, P. Zhang, S. Zhai, et al., Re-estimation of thermal contact resistance considering near-field thermal radiation effect [J], Applied Thermal Engineering 157 (2019) 113601.

[18] J.D. Anderson Jr, Hypersonic and High-Temperature Gas Dynamics [M], American Institute of Aeronautics and Astronautics, 2006.

[19] P.L. Roe, Approximate Riemann solvers, parameter vectors, and difference schemes [J], Journal of Computational Physics 43 (2) (1981) 357–372.

[20] S. Venkateswaran, C. Merkle, Dual time-stepping and preconditioning for unsteady computations [C], in: 33rd Aerospace Sciences Meeting and Exhibition, AIAA, Reno, NV, 1995, p. 78.

[21] Xu X, Lee J S, Pletcher R H. A compressible finite volume formulation for large eddy simulation of turbulent pipe flows at low Mach number in Cartesian coordinates[J]. Journal of Computational Physics, 2005, 203(1): 22-48.

[22] I. Abalakin, A. Dervieux, T.A. Kozubskaya, A vertex centered high order MUSCL scheme applying to linearised Euler acoustics [J], HAL-Inria, 2002.

[23] R. Ghias, R. Mittal, H. Dong, A sharp interface immersed boundary method for compressible viscous flows [J], Journal of Computational Physics 225 (1) (2007) 528–553.

[24] de Tullio M D, De Palma P, Iaccarino G, et al. An immersed boundary method for compressible flows using local grid refinement[J]. Journal of Computational Physics, 2007, 225(2): 2098-2117.

[25] C.G. Li, M. Tsubokura, R. Bale, Framework for simulation of natural convection in practical applications [J], International Communications in Heat and Mass Transfer 75 (2016) 52–58.

[26] Jia H, Gogos G. Laminar natural convection heat transfer from isothermal spheres[J]. International Journal of Heat and Mass Transfer, 1996, 39(8): 1603-1615.

[27] Tric E, Labrosse G, Betrouni M. A first incursion into the 3D structure of natural convection of air in a differentially heated cubic cavity, from accurate numerical solutions[J]. International Journal of Heat and Mass Transfer, 2000, 43(21): 4043-4056.

[28] Xu A, Shi L, Xi H D. Lattice Boltzmann simulations of three-dimensional thermal convective flows at high Rayleigh number[J]. International Journal of Heat and Mass Transfer, 2019, 140: 359-370.

[29] R.A. Kuyper, T.H. Van Der Meer, C.J. Hoogendoorn, et al., Numerical study of laminar and turbulent natural convection in an inclined square cavity [J], International Journal of Heat and Mass Transfer 36 (11) (1993) 2899–2911.

[30] T. Fusegi, J.M. Hyun, Laminar and transitional natural convection in an enclosure with complex and realistic conditions [J], International Journal of Heat and Fluid Flow 15 (4) (1994) 258–268.